Comparison of multiple tractography methods for reconstruction of the retinogeniculate visual pathway using diffusion MRI

Jianzhong He[1,2,*], Fan Zhang[2,*,&], Guoqiang Xie[2,3], Shun Yao[4,7], Yuanjing Feng[1,&], Dhiego C. A. Bastos[4], Yogesh Rathi[2,5], Nikos Makris[5,6], Ron Kikinis[2], Alexandra J. Golby[2,4], Lauren J. O'Donnell[2]

[1] Institution of Information Processing and Automation, Zhejiang University of Technology, Hangzhou, China
[2] Department of Radiology, Brigham and Women's Hospital, Harvard Medical School, Boston, USA
[3] Department of Neurosurgery, Nuclear Industry 215 Hospital of Shaanxi Province, Xianyang, China
[4] Department of Neurosurgery, Brigham and Women's Hospital, Harvard Medical School, Boston, USA
[5] Department of Psychiatry, Brigham and Women's Hospital, Harvard Medical School, Boston, USA
[6] Departments of Psychiatry, Neurology and Radiology, Massachusetts General Hospital, Harvard Medical School, Boston, USA
[7] Center for Pituitary Tumor Surgery, Department of Neurosurgery, The First Affiliated Hospital, Sun Yat-sen University, Guangzhou, China

* Co-first-authors; [&] Co-corresponding-authors

Abstract

The retinogeniculate visual pathway (RGVP) conveys visual information from the retina to the lateral geniculate nucleus. Anatomically, the RGVP can be separated into four subdivisions, including two decussating and two non-decussating fiber pathways, which cannot be identified by conventional magnetic resonance imaging (MRI). Diffusion MRI tractography has the potential to trace these subdivisions and is increasingly used to study the anatomy of the RGVP. However, it is not yet known which fiber tracking strategy is most suitable for tractographic reconstruction of the RGVP. In this study, four different tractography algorithms, including constrained spherical deconvolution (CSD) model based probabilistic (iFOD1) and deterministic (SD-Stream) methods, and multi-fiber (UKF-2T) and single-fiber (UKF-1T) unscented Kalman filter (UKF) tractography methods, are compared for reconstruction of the RGVP. Experiments are performed using diffusion MRI data of 57 subjects in the Human Connectome Project. The RGVP is identified using regions of interest created by two clinical experts. Anatomical measurements are used to assess the advantages and limitations of the four tracking strategies, including the reconstruction rate of the four RGVP subdivisions, the percentage of decussating fibers, the correlation between volumes of the traced RGVPs and a T1w-based RGVP segmentation, and an expert judgment to rank the anatomical appearance of the reconstructed RGVPs. Overall, we conclude that UKF-2T and iFOD1 produce the best RGVP reconstruction results. The iFOD1 method can better quantitatively estimate the percentage of decussating fibers, while the UKF-2T method produces reconstructed RGVPs that are judged to better correspond to the known anatomy.

Keywords: tractography, diffusion magnetic resonance imaging, Human Connectome Project, retinogeniculate visual pathway, cranial nerve

1. Introduction

The retinogeniculate pathway (RGVP) begins at the retina, passes through the optic nerve, the optic chiasm, and the optic tract, and finally connects to the lateral geniculate nucleus (LGN) (J. Salazar et al., 2019; Purves et al., 2001). See Figure 1 for an anatomical overview. Approximately 53-58 percent of RGVP fibers decussate (cross) at the optic chiasm (Chacko, 1948; Kupfer et al., 1967; v. Sántha, 1932). Therefore, the RGVP can be divided into four anatomical subdivisions: two decussating (medial) and two non-decussating (lateral) fiber pathways, and each subdivision undertakes the important task of conveying visual information of visual hemi-fields (Purves et al., 2014; Quigley et al., 1982; Quigley & Green, 1979).

The study of the RGVP is important in multiple research and clinical applications. The RGVP can be affected in many diseases, including pituitary tumors (Laws et al., 1977; Rucker & Kernohan, 1954), glioma (Hales et al., 2018), optic neuritis (Beck et al., 2003; Brex et al., 2002; Optic Neuritis Study Group, 1997), ischemic optic neuropathy (Attyé et al., 2018; Cho et al., 2016), and optic nerve sheath meningioma (Schick et al., 2004; Turbin et al., 2002). In particular, visualization of the RGVP can be helpful in planning surgical approaches to lesions intrinsic or extrinsic to the pathway. Neoplasms of the sellar region, such as pituitary adenomas, tuberculum sellae meningioma, Rathke's cleft cysts, and craniopharyngiomas can cause extrinsic compression of the RGVP fibers when extending superiorly (Ma et al., 2016). Optic pathway glioma (OPG), a childhood tumor most common in patients with neurofibromatosis type 1 (NF-1), is a diffusely infiltrative tumor with ill-defined boundaries, causing intrinsic compression and infiltration of the RGVP (Aquilina et al., 2015). Surgical resection of these tumors is challenging due to the high potential for damage to the visual apparatus. There is a poor correlation between tumor extent on conventional imaging modalities and visual impairment; therefore, detailed information about RGVP fiber pathway microstructure could potentially help clinicians in treatment decision making and surgical planning to potentially improve clinical outcomes (Aquilina et al., 2015; Fisher et al., 2012). The study of the complete RGVP is also relevant in the setting of high tension glaucoma, which can affect the whole optic pathway (Lestak et al., 2012).

Magnetic resonance imaging (MRI) techniques have been used to identify the RGVP for clinical and research purposes (Gala, 2015). Traditional T1-weighted (T1w) and T2-weighted (T2w) MRI are the most widely used, e.g, to compute the cross-sectional area of the intraorbital optic nerve (Gass et al., 1996; Simon J. Hickman, 2007; Simon J. Hickman et al., 2004; S. J. Hickman et al., 2001; Watanabe et al., 2008). However, these MRI sequences only indicate whether the RGVP is present at a particular location, while the 3D fiber pathway of the RGVP and the continuity of its subdivisions cannot be assessed. Diffusion MRI (dMRI), via a process called tractography, can track brain white matter and nerve fibers in vivo non-invasively based on the principle of detecting the random motion of water molecules in neural tissue (Basser et al., 1994, 2000). One advantage of dMRI is that it can enable tracking of the 3D trajectory of the RGVP for visualization of structures not visualized by traditional MRI sequences, e.g., crossing fibers at the optic chiasm (Puzniak et al., 2019). Multiple studies have investigated reconstruction of the RGVP using dMRI tractography (see Table 1) (Altıntaş et al., 2017; Ather et al., 2019; Hofer et al., 2010; Panesar et al., 2019; Yoshino et al., 2016).

Despite the wide use of dMRI for RGVP reconstruction, practical questions remain about which tractography methods can provide a comprehensive delineation of the RGVP fiber pathway. The RGVP is located within the complex skull base environment, which contains nerve, bone, air, soft tissue, and cerebrospinal fluid. These anatomical structures can result in partial voluming, where voxels contain mixed information from multiple components, and susceptibility artifacts, which affect nerve fiber tracking performance. In addition, a unique characteristic of the RGVP is that there are crossing nerve fibers at the optic chiasm, which requires a tractography method to be highly sensitive despite the presence of crossing fibers. Recent reviews came to the overall conclusion that the choice of tractography methods and/or parameter settings strongly affects cranial nerve fiber reconstruction, including the RGVP (Jacquesson, Frindel, et al., 2019; Shapey et al., 2019). Table 1 gives a summary of existing tractography-based RGVP studies to describe the current state of the art in terms of the fiber tracking methods being used, among which the standard diffusion tensor imaging (DTI) tractography and more advanced methods such as those using constrained spherical deconvolution (CSD) and generalized q-sampling imaging (GQI) are most widely used. While these studies have shown highly promising RGVP tracking performance, most have focused on certain RGVP subregions of interest, e.g., the optic nerve, the optic tract, and/or the RGVP fibers within the optic chiasm (as summarized in Table 1), but not the complete RGVP pathway .

The main contribution of this work is to investigate, for the first time, the performance of multiple tractography methods for reconstruction of the complete RGVP including the four anatomical subdivisions. Four different tractography methods are compared, including two methods based on the CSD model and two methods that use the unscented Kalman filter (UKF) tractography framework. We choose the CSD-based tractography methods because the CSD model is currently the most widely applied method for cranial nerve fiber tracking (Table 1), and we choose the UKF methods because UKF has recently shown high performance in reconstructing the cranial nerves (Xie et al., 2020a; Zhang, Xie, et al., 2020). A comprehensive quantitative and visual comparison is performed using dMRI data from the Human Connectome Project (HCP) (Glasser et al., 2013; Van Essen et al., 2013). Quantitative evaluation includes the reconstruction rate of the four anatomical subdivisions, the percentage of decussating fibers, and a comparison to anatomical-T1w-based RGVP segmentation. Furthermore, to assess the reliability of the RGVP tracking results, an inter-expert validation is performed to compare the spatial overlap of RGVPs reconstructed from two experts.

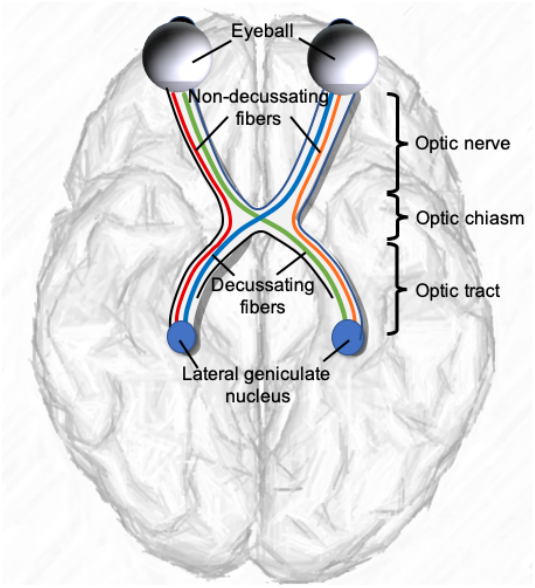

Figure 1. A schematic anatomical overview of the RGVP. There are four major subdivisions, including two non-decussating fiber pathways (orange and red) connecting the optic nerve and the optic tract in the same hemisphere and two decussating fiber pathways (green and blue) connecting the optic nerve and the optic tract across the hemispheres.

Table 1. Summary of published tractography studies of the RGVP and its subregions, organized according to the fiber reconstruction methods employed and the anatomical region studied.

Model & Tractography	**Anatomical Region Studied**	**Research**
DTI (deterministic)	OT	(Dasenbrock et al., 2011; Jin et al., 2019; Schmidt et al., 2018; M. Y. Takemura et al., 2017)
	ON and OT	(de Blank et al., 2013)
	RGVP	(Altıntaş et al., 2017; Hofer et al., 2010)
DTI (probabilistic)	ON	(Zolal et al., 2017)
	OT	(Backner et al., 2018; Frezzotti et al., 2016; Glick-Shames et al., 2019; Hoffmann et al., 2012; Levin et al., 2010; Malania et al., 2017; Maleki et al., 2012; Ogawa et al., 2014; N. Raz et al., 2015; Noa Raz et al., 2015; Noa Raz & Levin, 2014; H. Takemura et al., 2019)
	ON and OT	(Wu et al., 2019)
	RGVP	(Ather et al., 2019)
CSD (deterministic)	OT	(Hofstetter et al., 2019)
CSD (probabilistic)	ON	(Attyé et al., 2018; Miller et al., 2019)
	OC	(Puzniak et al., 2019)
	OT	(Haykal et al., 2019; Kammen et al., 2016; Rutland et al., 2019)

	ON and OT	(Allen et al., 2018; Hales et al., 2018)
	ON and OC	(Jacquesson, Frindel, et al., 2019)
GQI (deterministic)	ON	(Ho et al., 2019)
	OT	(Burton et al., 2018; Jin et al., 2019; Matsuo et al., 2018)
	RGVP	(Panesar et al., 2019; Yoshino et al., 2016)
Abbreviations: ON - optic nerve, OC - optic chiasm, OT - optic tract.		

2. Materials and Methods

2.1 Evaluation datasets

We used a total of 100 dMRI datasets (the "100 Unrelated Subjects" release) (54 females and 46 males, age: 22 to 35 years old) from the HCP database (https://www.humanconnectome.org) (Van Essen et al., 2013) for experimental evaluation. The HCP data scanning protocol was approved by the local Institutional Review Board (IRB) at Washington University. The HCP database provides dMRI data that was acquired with a high-quality image acquisition protocol using a customized Connectome Siemens Skyra scanner and processed using a well-designed processing pipeline (Glasser et al., 2013) including motion correction, eddy current correction, EPI distortion correction, and co-registration between dMRI and T1w data. The dMRI acquisition parameters in HCP were: TR=5520 ms, TE=89.5 ms, FA=78°, voxel size=1.25×1.25×1.25 mm^3, and FOV=210×180 mm^2. A total of 288 images were acquired in each dMRI dataset, including 18 baseline images with a low diffusion weighting b = 5 s/mm^2 and 270 diffusion weighted (DW) images evenly distributed at three shells of b = 1000/2000/3000 s/mm^2. In our study, we used the single-shell b=1000 s/mm^2 data, consisting of 90 DW images and 18 baseline images, to perform fiber tracking using each compared tractography method (see Section 2.2 for details). We chose single-shell b=1000 s/mm^2 data because it is similar to clinical acquisition protocols as applied in many previous RGVP-related studies (Lober et al., 2012; Maleki et al., 2012; Schmidt et al., 2018; Wu et al., 2019), and single-shell b=1000 s/mm^2 data has been shown in our previous study to be more effective for identification of cranial nerves than higher b values (Xie et al., 2020a). In addition, we also used the anatomical T1w data (co-registered with the dMRI), on which the RGVP was more visually apparent than on dMRI, for facilitating creation of tractography seeding masks (Section 2.2.1) and RGVP tracking performance evaluation (Section 2.3.4). The T1w image acquisition parameters were: TR=2400 ms, TE=2.14 ms, and voxel size=0.7×0.7×0.7 mm^3. More detailed information about the HCP data acquisition and preprocessing can be found in (Glasser et al., 2013).

To avoid potential effects on fiber tracking and experimental comparison, we performed a visual check of the dMRI data for each of the 100 subjects and we excluded any subjects whose dMRI data had incomplete RGVP coverage (as illustrated in Figure 2(a)) and/or abnormal signal that resulted in negative diffusion tensor eigenvalues (as illustrated in Figure 2(b)). For anonymization, face removal had been performed in the HCP imaging data using the algorithm as described in (Milchenko & Marcus, 2013). This process can cause a removal of dMRI data near the retina, such that only part of the RGVP is present in the data (see Figure 2(a) for an illustration in one example subject). We identified 38 subjects with incomplete RGVP coverage, which were excluded from our study. In addition, we excluded another 5 subjects with apparently abnormal signals in the skull base region where the RGVP passes through. In these subjects, we found many voxels with b=0 signals lower than the b=1000 signals, potentially due to Gibbs ringing effects and partial voluming issues (Veraart et al., 2016; Zhang, Ning, et al., 2019) resulted in negative diffusion tensor eigenvalues (see Figure 2(b) for an illustration in one example subject), which

could prevent fiber tracking of the RGVP. Overall, data from 57 subjects (male/female: 16/41; Age: 22-36) was included in our study.

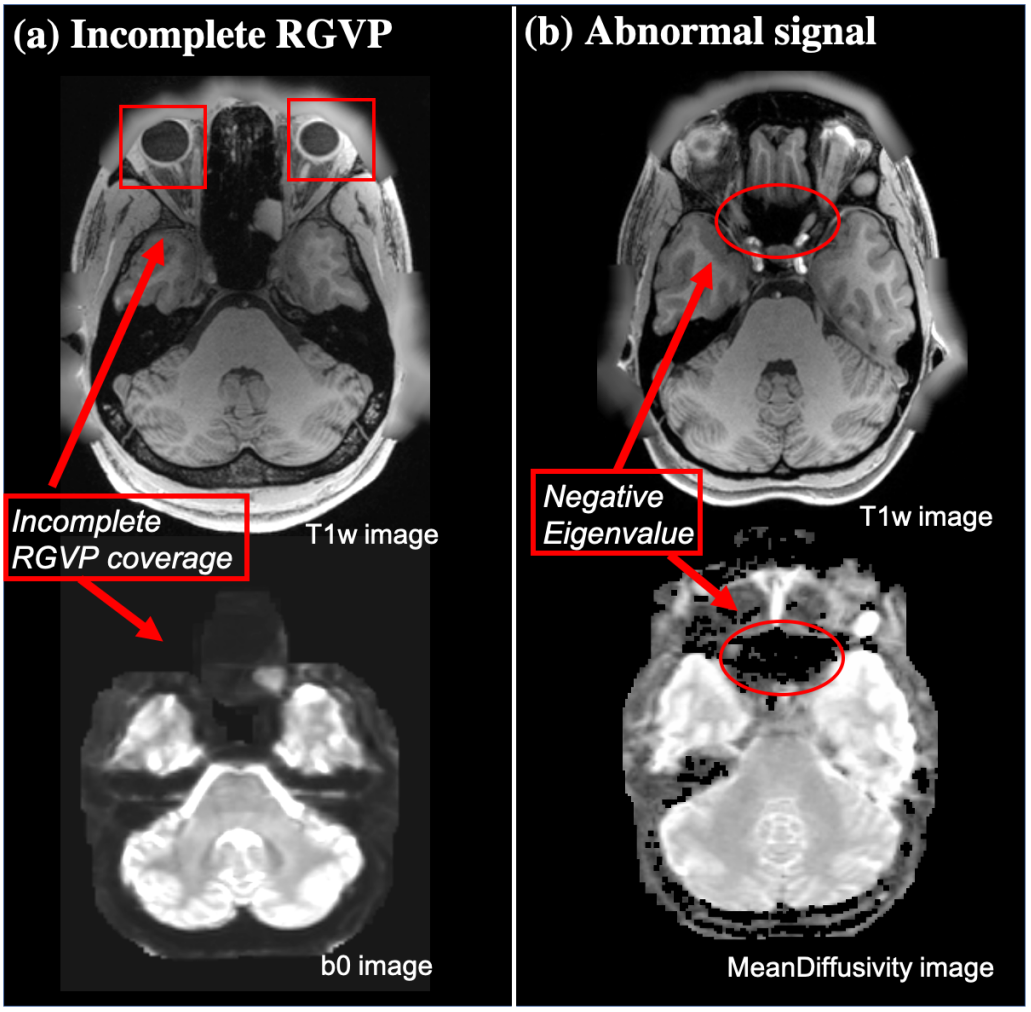

Figure 2. Illustration of two situations for excluded subjects. (a) shows an example of an incomplete RGVP in DWI data, where part of the optic nerve region is not present in the b0 image. (b) shows an example of abnormal signals, where the black holes on the mean diffusivity image show the voxels with negative diffusion tensor eigenvalues.

2.2 Four compared tractography methods

We compared four different tractography methods for reconstruction of the RGVP. The first two methods are *SD-Stream* and *iFOD1,* within the CSD tractography framework (Tournier et al., 2004, 2007, 2012). We chose the CSD framework because it has been widely used in cranial nerve studies (Allen et al., 2018; Attyé et al., 2018; Hales et al., 2018; Haykal et al., 2019; Miller et al., 2019; Puzniak et al., 2019; Schmidt et al., 2018; Xie et al., 2020a). In brief, in the CSD-based tractography framework, fiber tracking works by stepping along a particular direction at each tracking step, with a constraint on the angle between successive steps. The direction for each step is obtained by sampling the fiber orientation distribution (FOD) at the current point. The SD-Stream method performs deterministic tracking where fiber tracking follows only the local direction of the FOD amplitude peak, whereas the iFOD performs probabilistic tracking by choosing a random direction of FOD, such that the probability of a particular direction being produced is proportional to the amplitude of the FOD along that direction. The other two compared methods are *UKF-1T* and *UKF-2T*, within the UKF tractography framework (Z. Chen et al., 2016; Gong et al., 2018; Liao et al., 2017; Malcolm et al., 2010; Zhang et al., 2018; Zhang, Xie, et al., 2020) UKF tractography has been shown to be highly effective in reconstructing cranial nerves (Xie et al., 2020a; Zhang, Xie, et al.,

2020). It fits a tensor model to the diffusion data while tracking fibers, in a recursive estimation fashion (the current tracking estimate is guided by the previous one) using a Kalman filter. One benefit of the recursive estimation is to help stabilize model fitting; thus fiber tracking can be robust to a certain amount of imaging artifact/noise. In our study, we chose two types of UKF tractography. The UKF-1T method is a DTI tractography method, which fits a single tensor at each fiber tracking step, with the assumption that only one fiber passses through the current point. On the other hand, the UKF-2T method fits a mixture model of two tensors in which the first one represents the principal direction and the second one can represent crossing fibers.

2.2.1 Tractography seeding

RGVP tractography was seeded (initiated) from all voxels within a mask, which was larger than the possible region through which the RGVP passes. This procedure enabled comprehensive RGVP reconstruction and was restricted to the potential RGVP region for efficiency, as applied in our previous cranial nerve tractography studies (Xie et al., 2020a; Zhang, Xie, et al., 2020). To boost the creation of the tractography seeding mask for all 57 subjects under study, we performed semi-automated mask processing, as illustrated in Figure 3(a). First, we manually drew a mask that covered the RGVP region on a T1w template (downloaded at : http://nist.mni.mcgill.ca/?p=858) in MNI space (Grabner et al., 2006). Then, we transferred this mask to each subject under study using a non-linear registration between the subject's T1w data and the T1w template (FSL was used for computing the registration (Jenkinson et al., 2012)). In this way, the mask was transferred to each subject's dMRI space that was co-registered with the T1w data. We visually checked the computed mask for each subject.

Following the creation of the seeding mask, RGVP fiber tracking was performed using each compared tractography method. To compare across the different methods, we first performed an experiment to determine the best-performing parameters for each tractography method. The goal of this experiment was to provide an unbiased comparison across methods by identifying method-specific parameters that provide good tracking results, as in our previous work (Xie et al., 2020a). This step is critical because parameter settings will significantly influence the results of tractography (Parizel et al., 2007; H. Takemura et al., 2016; Wandell, 2016). Complete details for this experiment are provided in Supplementary Material 1. To briefly summarize, parameters affecting tractography starting and stopping were tested over a wide range of values. High-performing parameter combinations were identified according to their ability to track the four RGVP subdivisions. These final parameters for each tractography method are provided in Table 2. All other parameters of the tracking software packages were left as default. Overall, we generated the same number of fibers (n=40,000) using each tractography method, with a fiber length threshold of 45mm to eliminate any effect from fibers too short to form part of the RGVP anatomy.

Table 2. Best-performing parameters for each tractography method

Tractography Methods	**Tracking Parameters**
SD-Stream	*seedCutoff*=0.006, *stopCutoff*=0.005, *maximumAngle*=65
iFOD1	*seedCutoff*=0.011, *stopCutoff*=0.010, *maximumAngle*=10
UKF-1T	*SeedingFA*=0.02, *stoppingFA*=0.01, *Qm*=0.001, *Ql*=50
UKF-2T	*SeedingFA*=0.02, *stoppingFA*=0.01, *Qm*=0.001, *Ql*=50

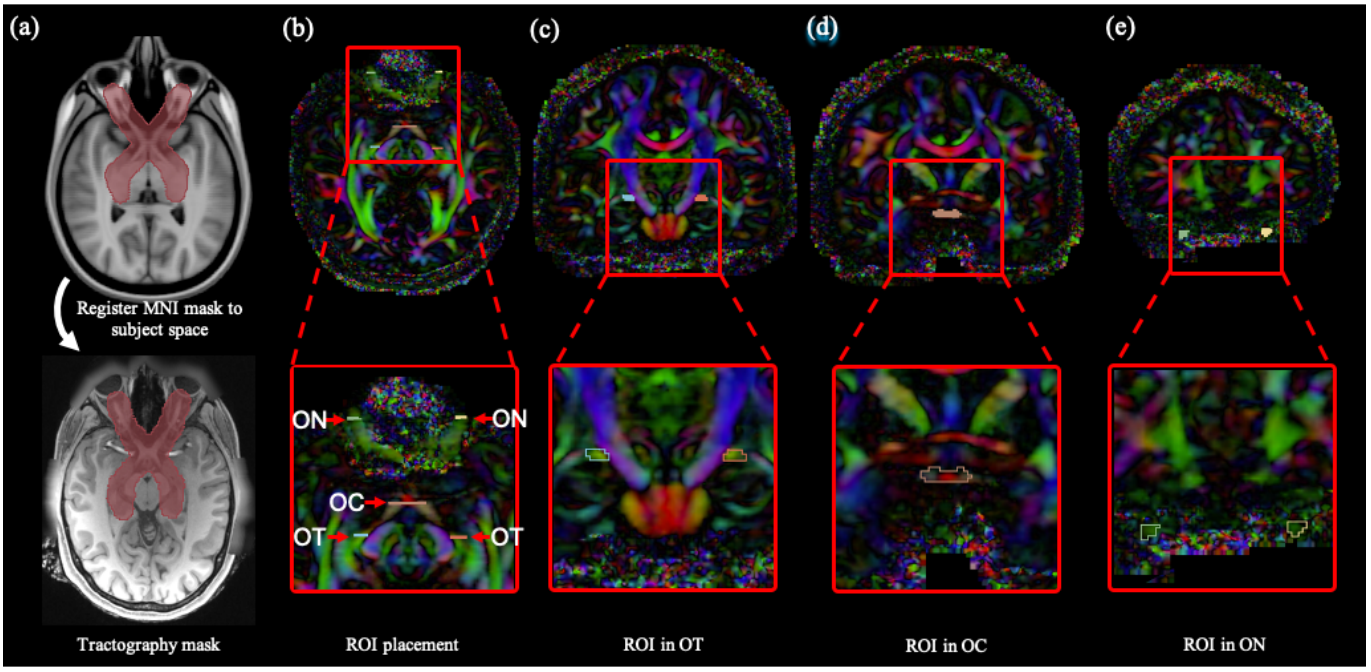

Figure 3. Tractography seeding mask and ROIs for selecting the RGVP fibers. (a) The tractography mask provides full coverage of the potential RGVP. (b) Five ROIs were drawn on the DTI image for every subject. (c) A pair of ROIs near the eyeball was drawn from the coronal view. (d) The second ROI was drawn at the optic chiasm. (e) The third ROIs were located in the optic tract near the LGN.

2.2.2 ROI-based RGVP fiber selection

Next, we performed an ROI-based selection of the RGVP fibers from the seeded tractography data for each compared fiber tracking method. Five ROIs were used, including two from the anterior part of the bilateral optic nerves (near the eyeballs), one from the optic chiasm, and two from the posterior part of the bilateral optic tracts (near the LGN), as illustrated in Figure 3 (b-e). Our choice of the bilateral optic nerve ROIs and the optic chiasm ROI was because they have been widely used for selection of optic nerve fibers (Maleki et al., 2012; Miller et al., 2019; H. Takemura et al., 2019). For identifying the optic tract fibers, we chose to use ROIs in the optic tract near the LGN. Accurately delineating the LGN with the current MRI imaging resolution is a challenging task. Most of the existing studies that perform optic tract fiber selection use ROIs that cover (much larger than) the LGN, followed by further manual fiber filtering of false positive fibers (Allen et al., 2018; Haykal et al., 2019; Maleki et al., 2012). In our study, in order to avoid potential bias from further manual fiber selection, we chose ROIs in the optic tract that were easily identified in HCP imaging data. For each of the 57 subjects under study, the five ROIs were drawn by an clinical expert (G.X., who is a practicing neurosurgeon) on the directionally encoded color (DEC) map computed from the dMRI data (as shown in Figure 3 (b-e)). (Note that a second set of ROIs per subject were drawn by another clinical expert (S.Y., who is a neurosurgeon), which were used for inter-expert reliability validation, as in Section 2.3.4.) Drawing ROIs directly on the dMRI data has been shown to be effective for RGVP fiber selection (Ather et al., 2019).

Selection of the RGVP fibers was performed using the obtained ROIs. Specifically, for each RGVP subdivision, three ROIs were used, including one of the optic nerve ROIs (left or right), one of the optic tract ROIs (left or right), and the optic chiasm ROI. In total, four fiber selections were performed to obtain the four anatomical RGVP subdivisions, as shown in Figure 4. For the rest of the paper, we refer to these subdivisions as LL (non-decussating fibers connecting left optic nerve and left optic tract), RR (non-decussating fibers connecting right optic nerve and right optic tract), LR (decussating fibers connecting left optic nerve and right optic tract), and RL (decussating fibers connecting right optic nerve and left optic tract).

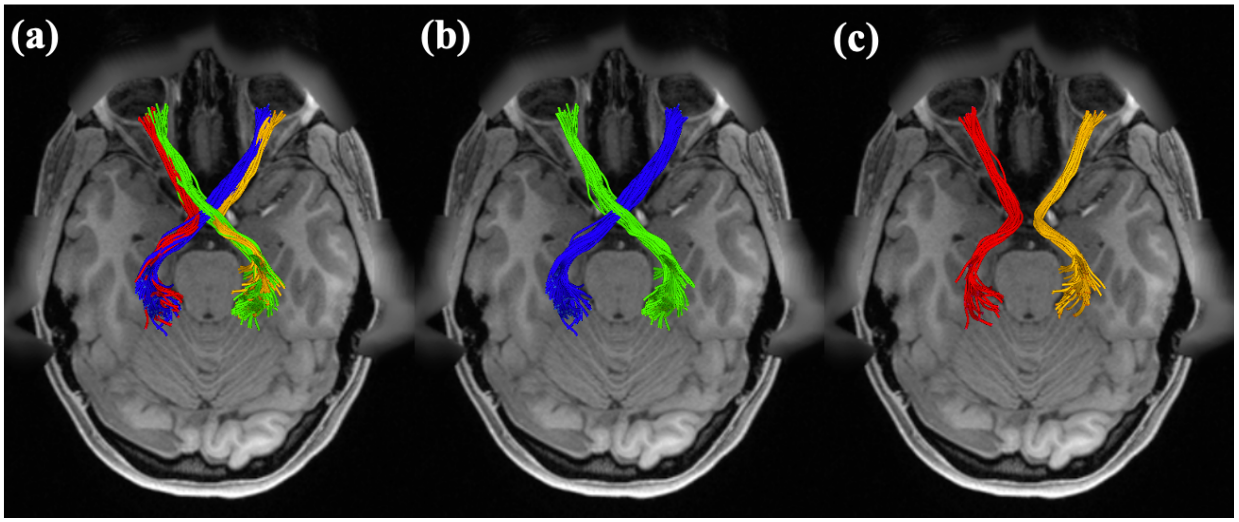

Figure 4. Illustration of the reconstructed subdivisions of the RGVP. (a) Axial view of an example RGVP overlaid on T1w image. Bundles of each color represent one subdivision. (b) A pair of decussating fiber bundles (green and blue), and (c) a pair of non-decussating fiber bundles (red and orange).

2.3 Experimental comparisons

We performed three experiments to assess the RGVP reconstruction performance of the different tractography methods. First, we compared the reconstruction rate of each RGVP subdivision across the methods (Section 2.3.1). Second, we computed the percentage of decussating fibers in the optic chiasm (Section 2.3.2), Third, we measured the correlation of the volumes of the RGVPs reconstructed with T1w-based RGVP segmentation (Section 2.3.3). In addition, to assess the reliability of the ROI selection, we performed an inter-expert reliability validation (Section 2.3.4).

2.3.1 Reconstruction rate of RGVP subdivisions

In this experiment, we assessed the ability of each tractography method to successfully reconstruct the four subdivisions of the RGVP. Specifically, for each RGVP subdivision (LL, RR, LR and RL), we considered that the fiber pathway was successfully traced if there was at least one fiber retained after ROI selection. Then, across all 57 subjects under study, the percentage of successfully traced pathways for each subdivision was computed as the reconstruction rate. In addition to the reconstruction rate per subdivision, we also computed the overall reconstruction rate for the full RGVP pathway (i.e., the percentage of subjects where all four RGVP subdivisions were successfully reconstructed). A statistical comparison was performed across the four tractography methods in terms of the overall reconstruction rate, as follows. A one-way repeated measures analysis of variance (ANOVA) was performed across the four methods. Following that, two-group Cochran's Q tests (Cochran, 1950) were performed between each pair of the four tractography methods (a total of 6 comparisons), with a false discovery rate (FDR) correction across the 6 comparisons. (Cochran's Q test is a non-parametric statistical comparison method for differences between two or more groups of matched samples, where each sample has a binary outcome, e.g. 0 and 1.)

2.3.2. Percentage of decussating fibers

In this experiment, we computed the percentage of the decussating and non-decussating fibers to compare the performance of the four tractography methods in the optic chiasm. It has been suggested that in neurotypical cases there are more decussating fibers than non-decussating fibers (approximately 53% to 58% of the RGVP fibers decussate at the optic chiasm (Chacko, 1948; Kupfer et al., 1967; v. Sántha, 1932)). As a result, multiple studies have investigated quantification of fiber decussation in the optic chiasm using tractography (Ather et al., 2019; Puzniak et al., 2019; Roebroeck et al., 2008; Staempfli et al., 2007). In our study, for each tractography method, we computed the percentage of decussating fibers per each

subject. A statistical comparison was performed across the four tractography methods, as follows. A one-way repeated measures analysis of variance (ANOVA) was computed across the four methods to determine whether they were statistically different from each other. Following that, we performed a post-hoc paired t-test between each pair of the four tractography methods (a total of 6 comparisons), with FDR correction across the 6 comparisons.

2.3.3 Correlation between T1w-based and tractography-based RGVP volumes

Anatomical T1w images have been widely used to estimate the volume of the RGVP (Simon J. Hickman et al., 2004; Kolbe et al., 2009; Ramli et al., 2014). In this experiment, we assessed the correlation of the volume of the RGVP reconstructed using tractography with T1w-based RGVP segmentation. For computing the volume of the T1w-based segmentation, first an RGVP segmentation was created on a T1w template image (MNI152) by a clinical expert (S.Y.), as shown in Figure 5. This RGVP segmentation was then applied to each individual subject using a registration between the T1w template and the subject-specific T1w data using FSL (Andersson et al., 2007). From the registered T1w-based segmentation, we computed the T1w-based RGVP volume. For computing the volume of the RGVP reconstructed using tractography, we created a normalized voxel-wise tract density map, where the value represents the number of fibers passing through each voxel divided by the maximum number of fibers across all voxels. This tract density map was converted into a binary map using a threshold of 0.05 to eliminate influence of voxels passed by only a few fibers (these are usually false positive fibers, and this procedure is widely used in other studies (Reid et al., 2020; Tian et al., 2018)). From this binary map, we computed the tractography-based RGVP volume. Then, for each tractography method, we computed Pearson's correlation between T1w-based and tractography-based RGVP volumes across all subjects. The correlation coefficient and the p-value are reported for each method.

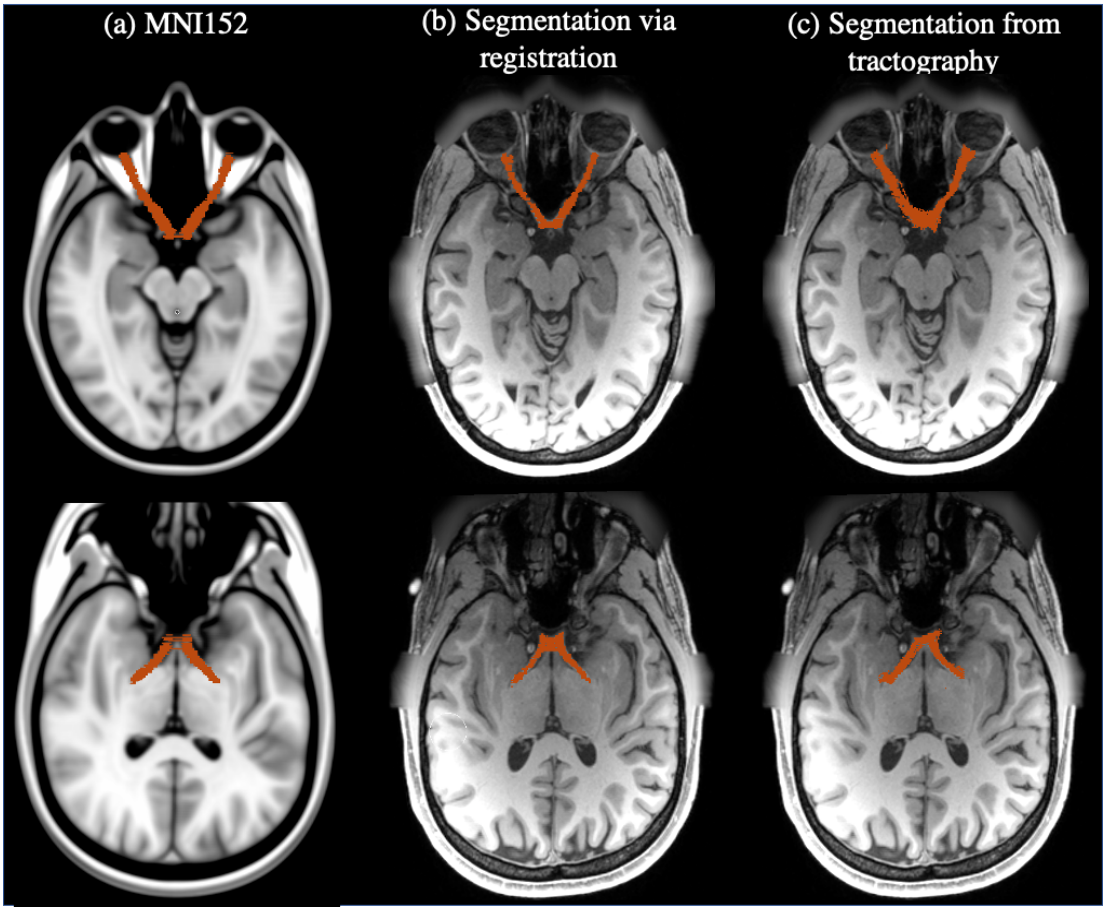

Figure 5. Visualization of RGVP segmentations. (a) shows the expert RGVP segmentation in MNI space; (b) shows a subject's RGVP segmentation, which was warped from the RGVP segmentation in MNI space. (c) shows a RGVP segmentation computed from tractography results.

2.3.4 Inter-expert validation

To assess the reliability of the RGVPs reconstructed for each tractography method, we conducted an inter-expert reliability validation. This experiment evaluated the spatial overlap of the RGVPs selected by two different experts. For each subject under study, a new set of ROIs was drawn by an additional expert (S.Y.) and used for a section of the second RGVP (as described in Section 2.2.2). Then, for the two RGVPs from the two experts, we computed the weighted Dice (wDice) coefficient (Cousineau et al., 2017a) to measure their spatial overlap. wDice is a metric designed specifically for measuring tract spatial overlap (Cousineau et al., 2017a; Zhang, Cetin Karayumak, et al., 2020; Zhang, Wu, et al., 2019). wDice extends the standard Dice coefficient (Dice, 1945) taking account of the number of fibers per voxel so that it gives higher weighting to voxels with dense fibers, as follows:

$$wDice(P_1, P_2) = \frac{\Sigma_{v'} W_{1,v'} + \Sigma_{v'} W_{2,v'}}{\Sigma_v W_{1,v} + \Sigma_v W_{2,v}} \quad (1)$$

Where P_1, P_2 represent two RGVPs selected using different expert-drawn ROIs, v' indicates the set of voxels that are within the intersection of the volumes of P_1 and P_2, v indicates the set of voxels that are within the union of the volumes of P_1 and P_2, and W is the fraction of the fibers passing through a voxel. A high wDice value represents a high reproducibility between the two RGVPs identified.

2.3.5 Expert judgment

We performed an expert judgment experiment to evaluate the quality of the RGVP reconstructions obtained by the four tractography methods, following the expert tract ranking method in our previous work (Gong et al., 2018). One expert (S.Y.) visually ranked the four RGVPs from each subject, as follows. The four tractography files were loaded into the 3D Slicer software (Kikinis et al., 2014; Norton et al., 2017; Zhang, Noh, et al., 2020), overlaid on the anatomical T1w and b0 images. The expert was blinded to the origin of each RGVP: tractography files were anonymized so that there was no information about which RGVP was from which tractography method. The overall RGVP reconstruction quality ranking was performed according to: 1) whether the reconstructed RGVP was anatomically reasonable as appearing on the T1w image, 2) whether there were apparent outlier fibers, and 3) whether the fiber density was sufficient to cover the RGVP pathway. The expert was asked to rank the four reconstructions based on his judgment, where a rank of 1 was the best and 4 was the worst. If two reconstructions were equally good or bad to the expert, these two RGVP reconstructions were given the same rank score. To summarize the expert judgment results, for each method, we then computed the mean and the standard deviation of the ranking scores.

3. Experimental results

3.1 Reconstruction rate of RGVP subdivisions

Figure 6 shows the reconstruction rate for each of the four RGVP subdivisions, as well as the overall reconstruction rate across all four subdivisions and all subjects. UKF-2T and iFOD1 generated the highest overall reconstruction rate, where all four subdivisions were reconstructed in 53 of 57 subjects (92.98%). This was followed by SD-Stream (70.18%), and UKF-1T (50.88%). The ANOVA comparison showed that the overall reconstruction rates were significantly different across the four methods. Post-hoc paired t-tests (with FDR correction) showed that the reconstruction rates of both UKF-2T and iFOD1 were significantly higher than UKF-1T and SD-Stream, while there were no significant differences between UKF-2T and iFOD1. The reconstruction rates of each RGVP subdivision showed the same pattern as the overall reconstruction rates (i.e., UKF-2T was the highest, followed by iFOD1, SD-Stream, and then UKF-1T), except for the LL subdivision where iFOD1 was higher than UKF-2T. In each of the UKF-2T, iFOD1 and SD-Stream methods, the reconstruction rates across the four subdivisions are similar, while in the UKF-1T methods, the reconstruction rates of the RL and LR subdivisions (decussating fibers) are lower than those of the LL and RR subdivisions (non-decussating fibers).

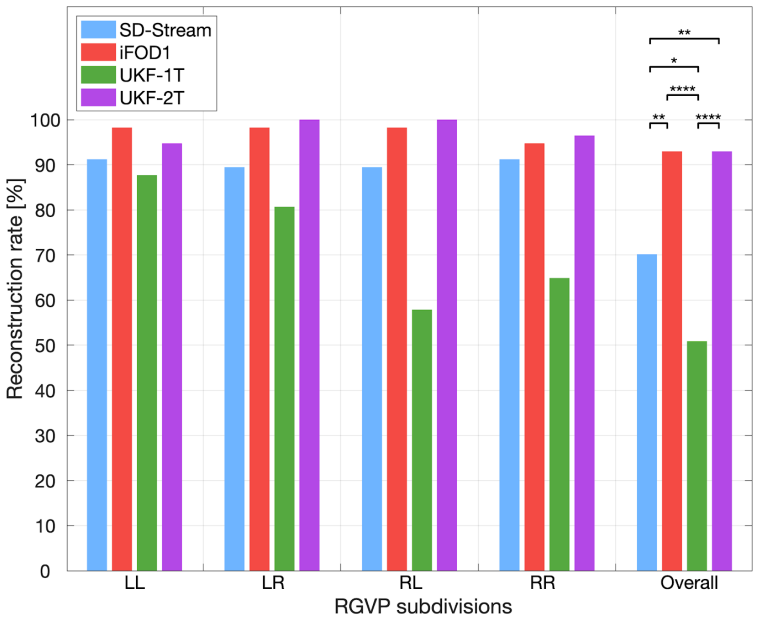

Figure 6. Reconstruction rate of RGVP subdivisions using different tractography methods. The overall RGVP reconstruction rates were statistically significantly different across the four compared tractography methods (ANOVA, p<0.0001). Post-hoc two-group Cochran's Q tests (with FDR correction) with significant results are indicated by asterisks. *: p<0.05; **: p<0.01; ****: p<0.0001.

3.2 Percentage of decussating fibers

Figure 7 gives the results for the percentage of decussating fibers obtained by each tractography method. The decussating percentages of UKF-2T and iFOD1 are higher than 50%, showing more decussating fibers than the non-decussating fibers (corresponding to the RGVP anatomy as reported in previous studies (Cajal, 1899; Chacko, 1948; Kupfer et al., 1967)), while the decussating percentages of SD-Stream and UKF-1T are lower than 50%.

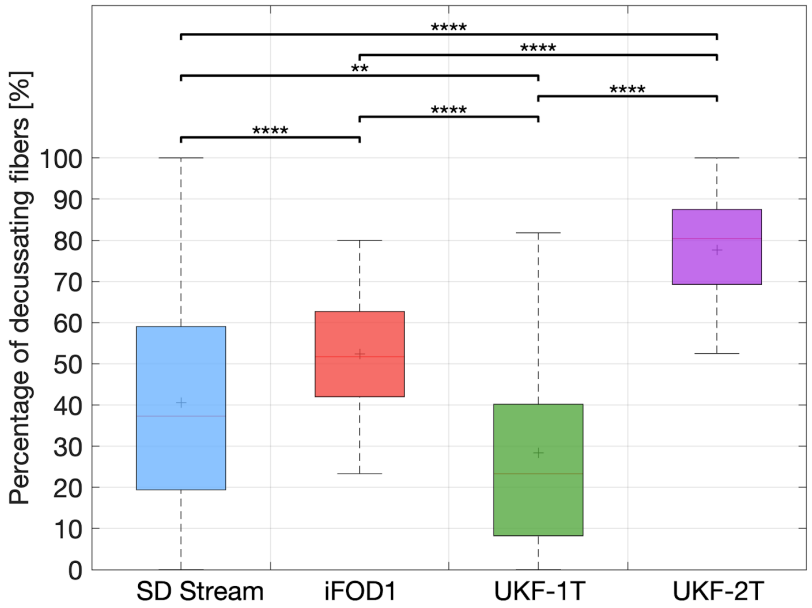

Figure 7. Boxplot indicates the percentage of decussating fibers of all subjects using each tractography method. On each box, the central line indicates the median, the plus symbol indicates the mean, and the bottom and top edges of the box indicate the 25th and 75th percentiles, respectively. The percentage of decussating fibers was statistically significantly different between the different tractography methods (ANOVA, p<0.0001). The Post-hoc paired t-tests (with FDR correction) with significant results are indicated by asterisks. **: p<0.01; ****: p<0.0001.

3.3 Correlation between T1w-based volume and tractography-based volume

Figure 8 gives the results of the correlation analysis between the T1w-based volume and the tractography-based volume of the RGVP. The SD-Stream and iFOD1 unexpectedly obtained negative correlations, while UKF-1T and UKF-2T obtained positive correlations. UKF-2T generated the highest correlation coefficient, representing the closest tractography-based volume compared to the T1w-based volume. There were no significant correlations in any of the four tractography methods.

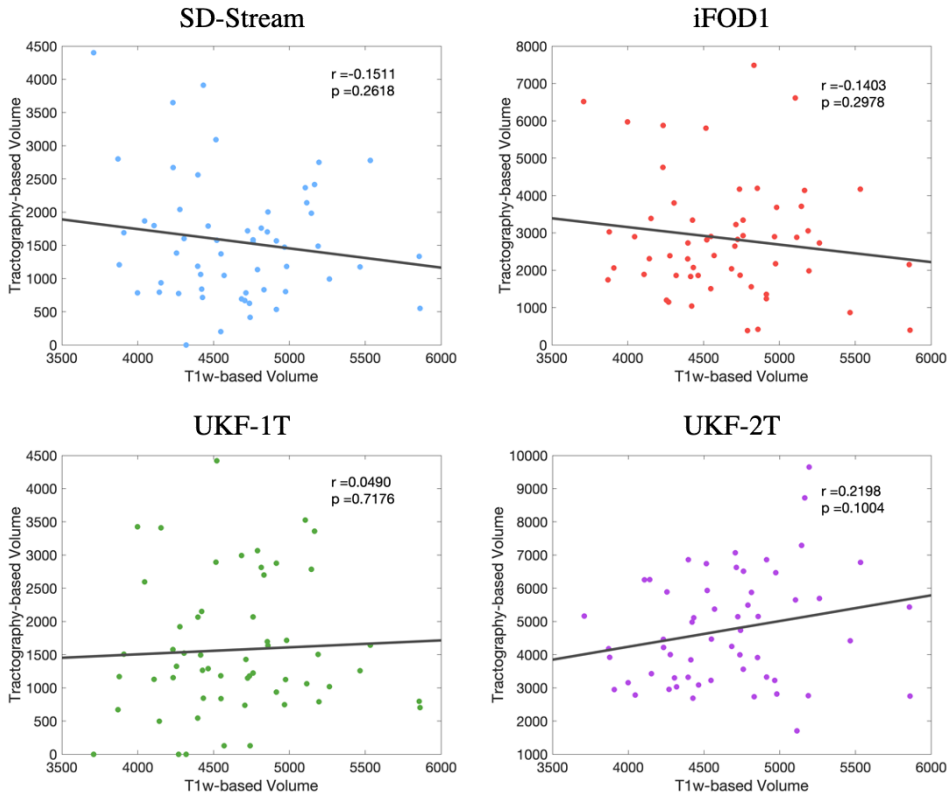

Figure 8. Scatter plots of correlation between T1w-based volume and tractography-based volume. The correlation coefficient *r* and the p-value are reported for each compared tractography method.

3.4 RGVP visualization

Figure 9 gives a visual comparison of the RGVP results using different tractography methods. In general, the CSD-based tractography methods (SD-Stream and iFOD1) generated a large number of visually apparent false positive fibers, while the UKF tractography methods (UKF-1T and UKF-2T) generated more anatomically plausible RGVP fibers, corresponding to the RGVP as appearing on the T1w image.

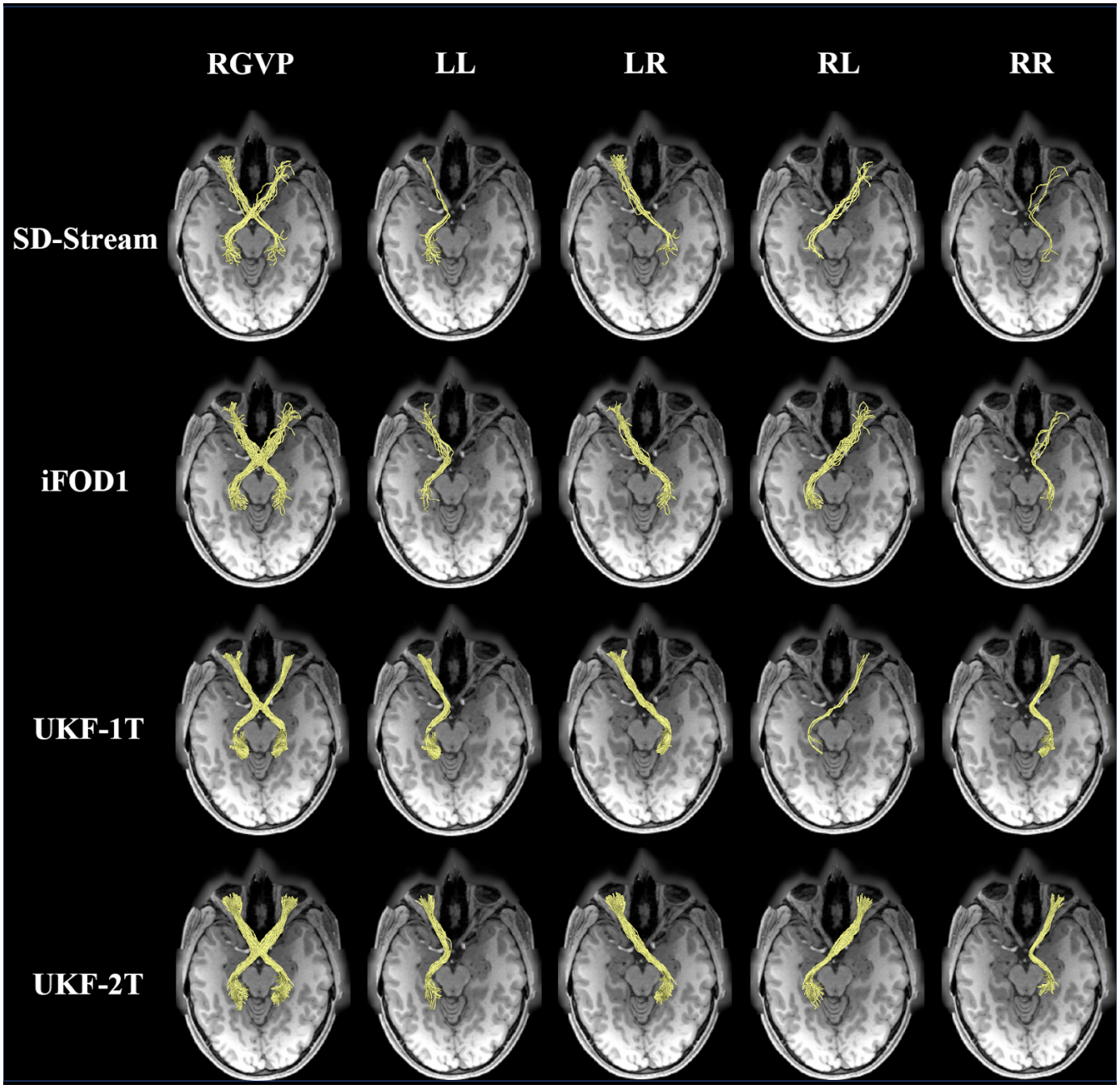

Figure 9. Visual comparison of the RGVP reconstructed using the four tractography methods. The RGVPs (yellow bundles) obtained from one HCP subject are displayed, overlaid on the T1w image. Each row shows the RGVP and its subdivisions using one of the tracking strategies. The first column shows the overall RGVP fiber pathway, and the following columns show the four subdivisions.

3.5 Inter-expert validation

Table 3 gives the inter-expert validation results. The wDice overlap scores of the two UKF tractography methods were the highest (over 0.81), followed by the SD-Stream method (0.77), while the iFOD1 method obtained the lowest wDice score (0.63) (wDice = 0.72 has been suggested to be a threshold for a good tract spatial overlap (Cousineau et al., 2017a)).

3.6 Expert judgment

Expert judgment was performed to rank the RGVP reconstructions of the 57 subjects under study. The rank could range from 1 to 4, where 1 was the best-judged reconstruction and 4 was the worst-judged reconstruction.The averaged ranking scores of the SD-Stream, iFOD1, UKF-1T and UKF-2T methods were

3.23 ± 0.74, 2.82 ± 0.72, 2.52 ± 1.33, and 1.34 ± 0.51, respectively. These results indicate that the UKF-2T method obtained the best expert evaluation performance in this experiment.

Table 3. Inter-expert validation results

Tractography methods	**Mean wDICE coefficient**
SD-Stream	0.77 ± 0.15
iFOD1	0.63 ± 0.11
UKF-1T	0.82 ± 0.19
UKF-2T	0.81 ± 0.09

4. Discussion

In this study, we proposed, for the first time, to investigate the performance of multiple tractography methods for reconstruction of the complete RGVP including the four anatomical subdivisions. We compared the RGVP reconstructions of four tractography methods, including deterministic (SD-Stream) and probabilistic (iFOD1) tractography based on the CSD model, and UKF tractography with one-tensor (UKF-1T) and two-tensor (UKF-2T) models. Anatomical measurements were conducted to assess the advantages and limitations of the four tractography methods for reconstructing RGVP. To this end, we computed the reconstruction rate of the four major RGVP subdivisions, the percentage of decussating fibers at the optic chiasm, and the correlation between the volumes of traced RGVPs and T1w-based RGVP segmentations. Finally, we performed an expert judgment experiment to rank the anatomical appearance of the reconstructed RGVPs. Overall, we have three main observations. First, across the four compared methods, we found that UKF-2T and iFOD1 obtained better performance than UKF-1T and SD-Stream. The RGVP reconstruction rates of UKF-2T and iFOD1 (about 92% in both methods) were significantly higher than UKF-1T and SD-Stream (50.88% and 70.18%, respectively). UKF-2T and iFOD1 also traced more decussating than non-decussating fibers in the optic chiasm, which is consistent with the findings of previous studies (approximately 53% to 58% as reported in (Chacko, 1948; Kupfer et al., 1967; v. Sántha, 1932)), whereas UKF-1T and SD-Stream trace more non-decussating fibers than decussating fibers. Second, comparing between UKF-2T and iFOD1, the percentage of decussating fibers in the iFOD1 method was more similar to the reported range in the previous studies, while the UKF-2T method obtained better volume correlation with the T1w-based RGVP segmentation. Third,the UKF-2T method obtained visually better RGVP pathways as appearing on the T1w image. Below, we discuss several detailed observations regarding the comparison results for the four tractography methods.

We found that multi-fiber tractography (UKF-2T) had advantages for reconstructing the complete RGVP compared to the single-fiber model (UKF-1T) within the UKF tractography framework. This is likely because a single-fiber model cannot estimate multiple fiber orientations (a well-known issue in the tractography literature (A. L. Alexander et al., 2001; D. C. Alexander, 2005; Behrens et al., 2007; Jeurissen et al., 2019; Tournier et al., 2004; Tuch et al., 2002)) in the region of the optic chiasm, where the decussating fibers cross. Multiple studies have suggested that multi-fiber models are beneficial for cranial nerve reconstruction (Behan et al., 2017; D. Q. Chen et al., 2016; Z. Chen et al., 2016; Xie et al., 2020a).

We found that probabilistic tractography (iFOD1) was more effective for reconstructing the RGVP than deterministic tractography (SD-Stream) within the CSD tractography framework. This is potentially because the deterministic tractography could only follow the principal orientation along the FOD amplitude peak, thus it could not effectively track through the skull base region where the signal-to-noise ratio (SNR) is low. On the other hand, the probabilistic tractography allowed fiber tracking along multiple orientations for

each FOD. Previous tractography-based cranial nerve studies have also shown the advantages of probabilistic tractography over traditional deterministic tractography, in particular, due to its good performance to handle the low SNR in the skull base (Jacquesson, Cotton, et al., 2019; Rueckriegel et al., 2016; Zolal et al., 2017).

Comparing between the UKF-2T and iFOD1 methods (the two methods that in general obtained the best RGVP reconstruction performance), the UKF-2T method produces reconstructed RGVPs that were judged to better correspond to known anatomy. The iFOD1 method performs tractography following randomly sampled directions. As a result, the traced fiber streamlines were highly curved, where certain fiber segments were outside the RGVP pathway (see Figure 9). In UKF-2T, each tracking step employs prior information from the previous step to help stabilize model fitting and includes a probabilistic prior about the rate of change of fiber orientation (defined as the parameter *Qm* introduced above). Consequently, sharp fiber curvatures are avoided as they are very unlikely, whereas fiber curvatures (e.g., curvature at the optic chiasm) supported by the dMRI are still allowed. Thus, UKF-2T generated highly smooth fiber streamlines that are the anatomically expected shape of the RGVP fibers as appearing on the T1w images.

Our inter-expert validation showed overall a high reliability of the RGVP reconstruction results. In particular, the wDice scores of UKF-1T, UKF-2T, and SD-Stream (0.82, 0.81 and 0.77, respectively) were over 0.72 that is a threshold for a good tract spatial overlap (Cousineau et al., 2017b). The wDice score for iFOD1 was relatively low (wDice = 0.63). This was most likely due to the fact that iFOD1 is a probabilistic tractography method and tends to generate fibers with certain fiber segments outside the RGVP pathway.

In this work, we performed what we believe is the first study to investigate the performance of multiple tractography methods for reconstruction of the complete RGVP including the four anatomical subdivisions. In the literature of tractography-based RGVP studies, most studies have focused on certain RGVP subregions of interest, e.g., the optic nerve, the optic tract, and/or the RGVP fibers within the optic chiasm (as summarized in Table 1). Several studies have shown successful tracking of the complete RGVP fiber pathway including the four major anatomical subdivisions (i.e., the two decussating and the two non-decussating fiber pathways) (Altıntaş et al., 2017; Hofer et al., 2010; Lober et al., 2012; Panesar et al., 2019; Yoshino et al., 2016). Some of these studies demonstrated that RGVP reconstruction could provide valuable information for pre-surgical planning. Nevertheless, these studies mostly present a visual demonstration, e.g., a visualization of RGVP fiber displacement due to tumors (Lober et al., 2012; Potgieser et al., 2014), without a comprehensive evaluation of different tractography methods. In this study, the higher reconstruction rate and high performance according to expert judgment indicated that UKF-2T is potentially a better tractography method for pre-surgical planning. Other previous studies (Ather et al., 2019; Puzniak et al., 2019) have reported the relationship between albinism and RGVP reconstruction results. However, the percentage of decussating fibers of these studies is underestimated compared to that known from histological studies (Chacko, 1948; Kupfer et al., 1967; v. Sántha, 1932). Our study showed that using iFOD1 reconstruction, the percentage of decussating fibers was close to the known anatomy (Chacko, 1948; Kupfer et al., 1967; v. Sántha, 1932).

Potential limitations of the present study, including suggested future work to address limitations, are as follows. First, in our current study, we focused on the assessment of the four major RGVP subdivisions, while it would be interesting to include more specific RGVP subregions. For example, it would be possible to investigate the RGVP fibers entering the superior colliculus (Purves et al., 2014). Second, we focused on RGVP tracking using dMRI data from healthy adults in the current study. Many research studies have suggested that the RGVP is important for understanding and/or potential treatment of various diseases, including glioma (Hales et al., 2018), optic neuritis (Beck et al., 2003; Brex et al., 2002; Optic Neuritis Study Group, 1997), ischemic optic neuropathy (Attyé et al., 2018; Cho et al., 2016), and sheath meningioma (Schick et al., 2004; Turbin et al., 2002). Further work could include a comparison of different tractography

methods on dMRI data from populations with neurological disorders or brain tumors. Third, false positive fiber tracking has been known to be prevalent in tractography (Maier-Hein et al., 2017; Thomas et al., 2014; Xie et al., 2020b). In our study, we have also observed several places where false positive RGVP tracking was likely to happen, in particular, at the RGVP endpoint regions (e.g., fiber tracking into the eyeballs and fiber tracking fanning before entering the LGN). A future investigation could include applying advanced fiber filtering techniques (Daducci et al., 2015; Miller et al., 2019; Pestilli et al., 2014; Smith et al., 2015) to further remove false positive fibers.

5. Conclusion

This is the first study to compare multiple tractography methods for reconstruction of the complete RGVP. Overall, we found that the multi-fiber UKF tractography (UKF-2T) and the probabilistic CSD tractography (iFOD1) obtained the best results, showing highly successful performance to identify the four major subdivisions of the RGVP. The iFOD1 method can better quantitatively estimate the percentage of decussating fibers, while the UKF-2T method produces reconstructed RGVPs that are judged to better correspond to known anatomy.

Acknowledgements:

We gratefully acknowledge funding provided by the following National Institutes of Health (NIH) grants: P41 EB015902, P41 EB015898, R01 MH074794, R01 MH111917, R01 MH119222, R01 CA235589, HHSN261200800001E, HHSN26100071, and U01 CA199459; the National Natural Science Foundation of China: 61976190, 61903336; Key Research & Development Project of Zhejiang Province grant: 2020C03070; Major Science and Technology Projects of Wenzhou: ZS2017007; Chinese Postdoctoral Science Foundation (2019M663271). Jianzhong He was supported by a scholarship from the China Scholarship Council (CSC).

References

Alexander, A. L., Hasan, K. M., Lazar, M., Tsuruda, J. S., & Parker, D. L. (2001). Analysis of partial volume effects in diffusion-tensor MRI. *Magnetic Resonance in Medicine: An Official Journal of the International Society for Magnetic Resonance in Medicine*, *45*(5), 770–780.

Alexander, D. C. (2005). Multiple-fiber reconstruction algorithms for diffusion MRI. *Annals of the New York Academy of Sciences*, *1064*, 113–133.

Allen, B., Schmitt, M. A., Kushner, B. J., & Rokers, B. (2018). Retinothalamic White Matter Abnormalities in Amblyopia. *Investigative Ophthalmology & Visual Science*, *59*(2), 921–929.

Altıntaş, Ö., Gümüştaş, S., Cinik, R., Anık, Y., Özkan, B., & Karabaş, L. (2017). Correlation of the measurements of optical coherence tomography and diffuse tension imaging of optic pathways in amblyopia. *International Ophthalmology*, *37*(1), 85–93.

Andersson, J. L. R., Jenkinson, M., & Smith, S. (2007). Non-linear registration aka Spatial normalisation FMRIB Technical Report TR07JA2. *FMRIB Analysis Group of the University of Oxford*, *28*, 1–22.

Aquilina, K., Daniels, D. J., Spoudeas, H., Phipps, K., Gan, H.-W., & Boop, F. A. (2015). Optic pathway glioma in children: does visual deficit correlate with radiology in focal exophytic lesions? *Child's Nervous System: ChNS: Official Journal of the International Society for Pediatric Neurosurgery*, *31*(11), 2041–2049.

Ather, S., Proudlock, F. A., Welton, T., Morgan, P. S., Sheth, V., Gottlob, I., & Dineen, R. A. (2019). Aberrant visual pathway development in albinism: From retina to cortex. *Human Brain Mapping*, *40*(3), 777–788.

Attyé, A., Jean, C., Remond, P., Peyrin, C., Lecler, A., Boudiaf, N., Aptel, F., Chiquet, C., Lamalle, L., & Krainik, A. (2018). Track-weighted imaging for neuroretina: Evaluations in healthy volunteers and ischemic optic neuropathy. *Journal of Magnetic Resonance Imaging: JMRI*, *48*(3), 737–747.

Backner, Y., Kuchling, J., Massarwa, S., Oberwahrenbrock, T., Finke, C., Bellmann-Strobl, J., Ruprecht, K., Brandt, A. U., Zimmermann, H., Raz, N., Paul, F., & Levin, N. (2018). Anatomical Wiring and Functional Networking Changes in the Visual System Following Optic Neuritis. *JAMA Neurology*, *75*(3), 287–295.

Basser, P. J., Mattiello, J., & LeBihan, D. (1994). MR diffusion tensor spectroscopy and imaging. *Biophysical Journal*, *66*(1), 259–267.

Basser, P. J., Pajevic, S., Pierpaoli, C., Duda, J., & Aldroubi, A. (2000). In vivo fiber tractography using DT-MRI data. *Magn. Reson. Med.*, *44*(4), 625–632.

Beck, R. W., Trobe, J. D., Moke, P. S., Gal, R. L., Xing, D., Bhatti, M. T., Brodsky, M. C., Buckley, E. G., Chrousos, G. A., & Corbett, J. (2003). High-and low-risk profiles for the development of multiple sclerosis within 10 years after optic neuritis: experience of the optic neuritis treatment trial. *Archives of Ophthalmology*, *121*(7), 944–949.

Behan, B., Chen, D. Q., Sammartino, F., DeSouza, D. D., Wharton-Shukster, E., & Hodaie, M. (2017). Comparison of Diffusion-Weighted MRI Reconstruction Methods for Visualization of Cranial Nerves in Posterior Fossa Surgery. *Frontiers in Neuroscience*, *11*, 554.

Behrens, T. E. J., Berg, H. J., Jbabdi, S., Rushworth, M. F. S., & Woolrich, M. W. (2007). Probabilistic diffusion tractography with multiple fibre orientations: What can we gain? *NeuroImage*, *34*(1), 144–155.

Brex, P. A., Ciccarelli, O., O'Riordan, J. I., Sailer, M., Thompson, A. J., & Miller, D. H. (2002). A longitudinal study of abnormalities on MRI and disability from multiple sclerosis. *The New England Journal of Medicine*, *346*(3), 158–164.

Burton, C. R., Schaeffer, D. J., Bobilev, A. M., Pierce, J. E., Rodrigue, A. L., Krafft, C. E., Clementz, B. A., Lauderdale, J. D., & McDowell, J. E. (2018). Microstructural differences in visual white matter tracts in people with aniridia. *Neuroreport*, *29*(17), 1473–1478.

Cajal, S. R. (1899). Die Struktur des Chiasma opticum. *Leipzig: Barth*.

Chacko, L. W. (1948). The laminar pattern of the lateral geniculate body in the primates. *Journal of Neurology, Neurosurgery, and Psychiatry*, *11*(3), 211–224.

Chen, D. Q., DeSouza, D. D., Hayes, D. J., Davis, K. D., O'Connor, P., & Hodaie, M. (2016). Diffusivity signatures characterize trigeminal neuralgia associated with multiple sclerosis. *Multiple Sclerosis* , *22*(1), 51–63.

Chen, Z., Tie, Y., Olubiyi, O., Zhang, F., Mehrtash, A., Rigolo, L., Kahali, P., Norton, I., Pasternak, O., Rathi, Y., Golby, A. J., & O'Donnell, L. J. (2016). Corticospinal tract modeling for neurosurgical planning by tracking through regions of peritumoral edema and crossing fibers using two-tensor unscented Kalman filter tractography. *International Journal of Computer Assisted Radiology and Surgery*, *11*(8), 1475–1486.

Cho, K. H., Ahn, S. J., Jung, C., Han, M. K., Park, K. H., & Woo, S. J. (2016). Ischemic Injury of the Papillomacular Bundle Is a Predictive Marker of Poor Vision in Eyes With Branch Retinal Artery Occlusion. *American Journal of Ophthalmology*, *162*, 107–120.e2.

Cochran, W. G. (1950). The comparison of percentages in matched samples. *Biometrika*, *37*(3-4), 256–266.

Cousineau, M., Jodoin, P.-M., Morency, F. C., Rozanski, V., Grand'Maison, M., Bedell, B. J., & Descoteaux, M. (2017a). A test-retest study on Parkinson's PPMI dataset yields statistically significant white matter fascicles. *NeuroImage. Clinical*, *16*, 222–233.

Cousineau, M., Jodoin, P.-M., Morency, F. C., Rozanski, V., Grand'Maison, M., Bedell, B. J., & Descoteaux, M. (2017b). A test-retest study on Parkinson's PPMI dataset yields statistically significant white matter fascicles. *NeuroImage. Clinical*, *16*, 222–233.

Daducci, A., Dal Palù, A., Lemkaddem, A., & Thiran, J.-P. (2015). COMMIT: Convex optimization modeling for microstructure informed tractography. *IEEE Transactions on Medical Imaging*, *34*(1), 246–257.

Dasenbrock, H. H., Smith, S. A., Ozturk, A., Farrell, S. K., Calabresi, P. A., & Reich, D. S. (2011). Diffusion tensor imaging of the optic tracts in multiple sclerosis: association with retinal thinning and visual disability. *Journal of Neuroimaging: Official Journal of the American Society of Neuroimaging*, *21*(2), e41–e49.

de Blank, P. M. K., Berman, J. I., Liu, G. T., Roberts, T. P. L., & Fisher, M. J. (2013). Fractional anisotropy of the optic radiations is associated with visual acuity loss in optic pathway gliomas of neurofibromatosis type 1. *Neuro-Oncology*, *15*(8), 1088–1095.

Dice, L. R. (1945). Measures of the Amount of Ecologic Association Between Species. *Ecology*, *26*(3), 297–302.

Fisher, M. J., Loguidice, M., Gutmann, D. H., Listernick, R., Ferner, R. E., Ullrich, N. J., Packer, R. J., Tabori, U., Hoffman, R. O., Ardern-Holmes, S. L., Hummel, T. R., Hargrave, D. R., Bouffet, E., Charrow, J., Bilaniuk, L. T., Balcer, L. J., & Liu, G. T. (2012). Visual outcomes in children with neurofibromatosis type 1-associated optic pathway glioma following chemotherapy: a multicenter retrospective analysis. In *Neuro-Oncology* (Vol. 14, Issue 6, pp. 790–797). https://doi.org/10.1093/neuonc/nos076

Frezzotti, P., Giorgio, A., Toto, F., De Leucio, A., & De Stefano, N. (2016). Early changes of brain connectivity in primary open angle glaucoma. *Human Brain Mapping*, *37*(12), 4581–4596.

Gala, F. (2015). Magnetic resonance imaging of optic nerve. *The Indian Journal of Radiology & Imaging*, *25*(4), 421–438.

Gass, A., Barker, G. J., Riordan-Eva, P., MacManus, D., Sanders, M., Tofts, P. S., McDonald, W. I., Moseley, I. F., & Miller, D. H. (1996). MRI of the optic nerve in benign intracranial hypertension. *Neuroradiology*, *38*(8), 769–773.

Glasser, M. F., Sotiropoulos, S. N., Wilson, J. A., Coalson, T. S., Fischl, B., Andersson, J. L., Xu, J., Jbabdi, S., Webster, M., Polimeni, J. R., Van Essen, D. C., Jenkinson, M., & WU-Minn HCP Consortium. (2013). The minimal preprocessing pipelines for the Human Connectome Project. *NeuroImage*, *80*, 105–124.

Glick-Shames, H., Backner, Y., Bick, A., Raz, N., & Levin, N. (2019). The impact of localized grey matter damage on neighboring connectivity: posterior cortical atrophy and the visual network. *Brain Imaging and Behavior*, *13*(5), 1292–1301.

Gong, S., Zhang, F., Norton, I., Essayed, W. I., Unadkat, P., Rigolo, L., Pasternak, O., Rathi, Y., Hou, L., Golby, A. J., & O'Donnell, L. J. (2018). Free water modeling of peritumoral edema using multi-fiber tractography: Application to tracking the arcuate fasciculus for neurosurgical planning. *PloS One*, *13*(5), e0197056.

Grabner, G., Janke, A. L., Budge, M. M., Smith, D., Pruessner, J., & Collins, D. L. (2006). Symmetric atlasing and model based segmentation: an application to the hippocampus in older adults. *Medical Image Computing and Computer-Assisted Intervention: MICCAI ... International Conference on Medical Image Computing and Computer-Assisted Intervention*, *9*(Pt 2), 58–66.

Hales, P. W., Smith, V., Dhanoa-Hayre, D., O'Hare, P., Mankad, K., d'Arco, F., Cooper, J., Kaur, R., Phipps, K., Bowman, R., Hargrave, D., & Clark, C. (2018). Delineation of the visual pathway in paediatric optic pathway glioma patients using probabilistic tractography, and correlations with visual acuity. *NeuroImage. Clinical*, *17*, 541–548.

Haykal, S., Curcic-Blake, B., Jansonius, N. M., & Cornelissen, F. W. (2019). Fixel-Based Analysis of Visual Pathway White Matter in Primary Open-Angle Glaucoma. *Investigative Ophthalmology & Visual Science*, *60*(12), 3803–3812.

Hickman, S. J. (2007). Optic nerve imaging in multiple sclerosis. *Journal of Neuroimaging: Official Journal of the American Society of Neuroimaging*, *17 Suppl 1*, 42S – 45S.

Hickman, S. J., Brex, P. A., Brierley, C. M., Silver, N. C., Barker, G. J., Scolding, N. J., Compston, D. A., Moseley, I. F., Plant, G. T., & Miller, D. H. (2001). Detection of optic nerve atrophy following a single episode of unilateral optic neuritis by MRI using a fat-saturated short-echo fast FLAIR sequence. *Neuroradiology*, *43*(2), 123–128.

Hickman, S. J., Toosy, A. T., Jones, S. J., Altmann, D. R., Miszkiel, K. A., MacManus, D. G., Barker, G. J., Plant, G. T., Thompson, A. J., & Miller, D. H. (2004). A serial MRI study following optic nerve mean area in acute optic neuritis. *Brain: A Journal of Neurology*, *127*(Pt 11), 2498–2505.

Ho, C. Y., Deardorff, R., Kralik, S. F., West, J. D., Wu, Y.-C., & Shih, C.-S. (2019). Comparison of multi-shot and single shot echo-planar diffusion tensor techniques for the optic pathway in patients with

neurofibromatosis type 1. *Neuroradiology*, *61*(4), 431–441.

Hofer, S., Karaus, A., & Frahm, J. (2010). Reconstruction and dissection of the entire human visual pathway using diffusion tensor MRI. *Frontiers in Neuroanatomy*, *4*, 15.

Hoffmann, M. B., Kaule, F. R., Levin, N., Masuda, Y., Kumar, A., Gottlob, I., Horiguchi, H., Dougherty, R. F., Stadler, J., Wolynski, B., Speck, O., Kanowski, M., Liao, Y. J., Wandell, B. A., & Dumoulin, S. O. (2012). Plasticity and stability of the visual system in human achiasma. *Neuron*, *75*(3), 393–401.

Hofstetter, S., Sabbah, N., Mohand-Saïd, S., Sahel, J.-A., Habas, C., Safran, A. B., & Amedi, A. (2019). The development of white matter structural changes during the process of deterioration of the visual field. *Scientific Reports*, *9*(1), 2085.

Jacquesson, T., Cotton, F., Attyé, A., Zaouche, S., Tringali, S., Bosc, J., Robinson, P., Jouanneau, E., & Frindel, C. (2019). Probabilistic Tractography to Predict the Position of Cranial Nerves Displaced by Skull Base Tumors: Value for Surgical Strategy Through a Case Series of 62 Patients. *Neurosurgery*, *85*(1), E125–E136.

Jacquesson, T., Frindel, C., Kocevar, G., Berhouma, M., Jouanneau, E., Attyé, A., & Cotton, F. (2019). Overcoming Challenges of Cranial Nerve Tractography: A Targeted Review. *Neurosurgery*, *84*(2), 313–325.

Jenkinson, M., Beckmann, C. F., Behrens, T. E. J., Woolrich, M. W., & Smith, S. M. (2012). FSL. *NeuroImage*, *62*(2), 782–790.

Jeurissen, B., Descoteaux, M., Mori, S., & Leemans, A. (2019). Diffusion MRI fiber tractography of the brain. *NMR in Biomedicine*, *32*(4), e3785.

Jin, Z., Bao, Y., Wang, Y., Li, Z., Zheng, X., Long, S., & Wang, Y. (2019). Differences between generalized Q-sampling imaging and diffusion tensor imaging in visualization of crossing neural fibers in the brain. *Surgical and Radiologic Anatomy: SRA*, *41*(9), 1019–1028.

J. Salazar, J., I. Ramírez, A., De Hoz, R., Salobrar-Garcia, E., Rojas, P., A. Fernández-Albarral, J., López-Cuenca, I., Rojas, B., Triviño, A., & M. Ramírez, J. (2019). Anatomy of the Human Optic Nerve: Structure and Function. In F. M. Ferreri (Ed.), *Optic Nerve*. IntechOpen.

Kammen, A., Law, M., Tjan, B. S., Toga, A. W., & Shi, Y. (2016). Automated retinofugal visual pathway reconstruction with multi-shell HARDI and FOD-based analysis. *NeuroImage*, *125*, 767–779.

Kikinis, R., Pieper, S. D., & Vosburgh, K. G. (2014). 3D Slicer: A Platform for Subject-Specific Image Analysis, Visualization, and Clinical Support. In F. A. Jolesz (Ed.), *Intraoperative Imaging and Image-Guided Therapy* (pp. 277–289). Springer New York.

Kolbe, S., Chapman, C., Nguyen, T., Bajraszewski, C., Johnston, L., Kean, M., Mitchell, P., Paine, M., Butzkueven, H., Kilpatrick, T., & Egan, G. (2009). Optic nerve diffusion changes and atrophy jointly predict visual dysfunction after optic neuritis. *NeuroImage*, *45*(3), 679–686.

Kupfer, C., Chumbley, L., & Downer, J. C. (1967). Quantitative histology of optic nerve, optic tract and lateral geniculate nucleus of man. *Journal of Anatomy*, *101*(Pt 3), 393–401.

Laws, E. R., Jr, Trautmann, J. C., & Hollenhorst, R. W., Jr. (1977). Transsphenoidal decompression of the optic nerve and chiasm. Visual results in 62 patients. *Journal of Neurosurgery*, *46*(6), 717–722.

Lestak, J., Nutterova, E., Pitrova, S., Krejcova, H., Bartosova, L., & Forgacova, V. (2012). High tension versus normal tension glaucoma. *A Comparison of Structural and Functional Examinations. J Clinic Experiment Ophthalmol S*, *5*, 2.

Levin, N., Dumoulin, S. O., Winawer, J., Dougherty, R. F., & Wandell, B. A. (2010). Cortical maps and white matter tracts following long period of visual deprivation and retinal image restoration. *Neuron*, *65*(1), 21–31.

Liao, R., Ning, L., Chen, Z., Rigolo, L., Gong, S., Pasternak, O., Golby, A. J., Rathi, Y., & O'Donnell, L. J. (2017). Performance of unscented Kalman filter tractography in edema: Analysis of the two-tensor model. *NeuroImage. Clinical*, *15*, 819–831.

Lober, R. M., Guzman, R., Cheshier, S. H., Fredrick, D. R., Edwards, M. S. B., & Yeom, K. W. (2012). Application of diffusion tensor tractography in pediatric optic pathway glioma: Clinical article. *Journal of Neurosurgery. Pediatrics*, *10*(4), 273–280.

Maier-Hein, K. H., Neher, P. F., Houde, J.-C., Côté, M.-A., Garyfallidis, E., Zhong, J., Chamberland, M., Yeh, F.-C., Lin, Y.-C., Ji, Q., Reddick, W. E., Glass, J. O., Chen, D. Q., Feng, Y., Gao, C., Wu, Y., Ma, J., He, R., Li, Q., … Descoteaux, M. (2017). The challenge of mapping the human connectome based on diffusion tractography. *Nature Communications*, *8*(1), 1349.

Ma, J., Su, S., Yue, S., Zhao, Y., Li, Y., Chen, X., & Ma, H. (2016). Preoperative Visualization of Cranial Nerves in Skull Base Tumor Surgery Using Diffusion Tensor Imaging Technology. *Turkish Neurosurgery*, *26*(6), 805–812.

Malania, M., Konrad, J., Jägle, H., Werner, J. S., & Greenlee, M. W. (2017). Compromised Integrity of Central Visual Pathways in Patients With Macular Degeneration. *Investigative Ophthalmology & Visual Science*, *58*(7), 2939–2947.

Malcolm, J. G., Shenton, M. E., & Rathi, Y. (2010). Filtered multitensor tractography. *IEEE Transactions on Medical Imaging*, *29*(9), 1664–1675.

Maleki, N., Becerra, L., Upadhyay, J., Burstein, R., & Borsook, D. (2012). Direct optic nerve pulvinar connections defined by diffusion MR tractography in humans: implications for photophobia. *Human Brain Mapping*, *33*(1), 75–88.

Matsuo, S., Baydin, S., Güngör, A., Middlebrooks, E. H., Komune, N., Iihara, K., & Rhoton, A. L. (2018). Prevention of postoperative visual field defect after the occipital transtentorial approach: anatomical study. *Journal of Neurosurgery*, *129*(1), 188–197.

Milchenko, M., & Marcus, D. (2013). Obscuring surface anatomy in volumetric imaging data. *Neuroinformatics*, *11*(1), 65–75.

Miller, N., Liu, Y., Krivochenitser, R., & Rokers, B. (2019). Linking neural and clinical measures of glaucoma with diffusion magnetic resonance imaging (dMRI). *PloS One*, *14*(5), e0217011.

Norton, I., Essayed, W. I., Zhang, F., Pujol, S., Yarmarkovich, A., Golby, A. J., Kindlmann, G., Wassermann, D., Estepar, R. S. J., Rathi, Y., Pieper, S., Kikinis, R., Johnson, H. J., Westin, C.-F., & O'Donnell, L. J. (2017). SlicerDMRI: Open Source Diffusion MRI Software for Brain Cancer Research. *Cancer Research*, *77*(21), e101–e103.

Ogawa, S., Takemura, H., Horiguchi, H., Terao, M., Haji, T., Pestilli, F., Yeatman, J. D., Tsuneoka, H., Wandell, B. A., & Masuda, Y. (2014). White matter consequences of retinal receptor and ganglion cell damage. *Investigative Ophthalmology & Visual Science*, *55*(10), 6976–6986.

Optic Neuritis Study Group. (1997). The 5-year risk of MS after optic neuritis. Experience of the optic neuritis treatment trial. *Neurology*, *49*(5), 1404–1413.

Panesar, S. S., Abhinav, K., Yeh, F.-C., Jacquesson, T., Collins, M., & Fernandez-Miranda, J. (2019). Tractography for Surgical Neuro-Oncology Planning: Towards a Gold Standard. *Neurotherapeutics: The Journal of the American Society for Experimental NeuroTherapeutics*, *16*(1), 36–51.

Parizel, P. M., Van Rompaey, V., Van Loock, R., Van Hecke, W., Van Goethem, J. W., Leemans, A., & Sijbers, J. (2007). Influence of user-defined parameters on diffusion tensor tractography of the corticospinal tract. *The Neuroradiology Journal*, *20*(2), 139–147.

Pestilli, F., Yeatman, J. D., Rokem, A., Kay, K. N., & Wandell, B. A. (2014). Evaluation and statistical inference for human connectomes. *Nature Methods*, *11*(10), 1058–1063.

Potgieser, A. R. E., Wagemakers, M., van Hulzen, A. L. J., de Jong, B. M., Hoving, E. W., & Groen, R. J. M. (2014). The role of diffusion tensor imaging in brain tumor surgery: a review of the literature. *Clinical Neurology and Neurosurgery*, *124*, 51–58.

Purves, D., Augustine, G. J., Fitzpatrick, D., Hall, W. C., LaMantia, A. S., McNamara, J. O., & White, L. (2014). Neuroscience, 2008. *De Boeck, Sinauer, Sunderland, Mass*, 15–16.

Purves, D., Augustine, G. J., Fitzpatrick, D., Katz, L. C., LaMantia, A.-S., McNamara, J. O., & Mark Williams, S. (2001). *Central Projections of Retinal Ganglion Cells*. Sinauer Associates.

Puzniak, R. J., Ahmadi, K., Kaufmann, J., Gouws, A., Morland, A. B., Pestilli, F., & Hoffmann, M. B. (2019). Quantifying nerve decussation abnormalities in the optic chiasm. *NeuroImage. Clinical*, *24*, 102055.

Quigley, H. A., Addicks, E. M., & Green, W. R. (1982). Quantitative correlation of nerve fiber loss and visual field defect in glaucoma, ischemic neuropathy, papilledema, and toxic neuropathy. *Archives of*

Ophthalmology, *100*(1), 135–146.

Quigley, H. A., & Green, W. R. (1979). The histology of human glaucoma cupping and optic nerve damage: clinicopathologic correlation in 21 eyes. *Ophthalmology*, *86*(10), 1803–1830.

Ramli, N. M., Sidek, S., Rahman, F. A., Peyman, M., Zahari, M., Rahmat, K., & Ramli, N. (2014). Novel use of 3T MRI in assessment of optic nerve volume in glaucoma. *Graefe's Archive for Clinical and Experimental Ophthalmology = Albrecht von Graefes Archiv Fur Klinische Und Experimentelle Ophthalmologie*, *252*(6), 995–1000.

Raz, N., Bick, A. S., Ben-Hur, T., & Levin, N. (2015). Focal demyelinative damage and neighboring white matter integrity: an optic neuritis study. *Multiple Sclerosis* , *21*(5), 562–571.

Raz, N., Bick, A. S., Klistorner, A., Spektor, S., Reich, D. S., Ben-Hur, T., & Levin, N. (2015). Physiological Correlates and Predictors of Functional Recovery After Chiasmal Decompression. *Journal of Neuro-Ophthalmology: The Official Journal of the North American Neuro-Ophthalmology Society*, *35*(4), 348–352.

Raz, N., & Levin, N. (2014). Cortical and white matter mapping in the visual system-more than meets the eye: on the importance of functional imaging to understand visual system pathologies. *Frontiers in Integrative Neuroscience*, *8*, 68.

Reid, L. B., Cespedes, M. I., & Pannek, K. (2020). How many streamlines are required for reliable probabilistic tractography? Solutions for microstructural measurements and neurosurgical planning. *NeuroImage*, *211*, 116646.

Roebroeck, A., Galuske, R., Formisano, E., Chiry, O., Bratzke, H., Ronen, I., Kim, D.-S., & Goebel, R. (2008). High-resolution diffusion tensor imaging and tractography of the human optic chiasm at 9.4 T. *NeuroImage*, *39*(1), 157–168.

Rucker, C. W., & Kernohan, J. W. (1954). Notching of the optic chiasm by overlying arteries in pituitary tumors. *A.M.A. Archives of Ophthalmology*, *51*(2), 161–170.

Rueckriegel, S. M., Homola, G. A., Hummel, M., Willner, N., Ernestus, R.-I., & Matthies, C. (2016). Probabilistic Fiber-Tracking Reveals Degeneration of the Contralateral Auditory Pathway in Patients with Vestibular Schwannoma. *AJNR. American Journal of Neuroradiology*, *37*(9), 1610–1616.

Rutland, J. W., Padormo, F., Yim, C. K., Yao, A., Arrighi-Allisan, A., Huang, K.-H., Lin, H.-M., Chelnis, J., Delman, B. N., Shrivastava, R. K., & Balchandani, P. (2019). Quantitative assessment of secondary white matter injury in the visual pathway by pituitary adenomas: a multimodal study at 7-Tesla MRI. *Journal of Neurosurgery*, *132*(2), 333–342.

Schick, U., Dott, U., & Hassler, W. (2004). Surgical management of meningiomas involving the optic nerve sheath. *Journal of Neurosurgery*, *101*(6), 951–959.

Schmidt, M. A., Knott, M., Heidemann, R., Michelson, G., Kober, T., Dörfler, A., & Engelhorn, T. (2018). Investigation of lateral geniculate nucleus volume and diffusion tensor imaging in patients with normal tension glaucoma using 7 tesla magnetic resonance imaging. *PloS One*, *13*(6), e0198830.

Shapey, J., Vos, S. B., Vercauteren, T., Bradford, R., Saeed, S. R., Bisdas, S., & Ourselin, S. (2019). Clinical Applications for Diffusion MRI and Tractography of Cranial Nerves Within the Posterior Fossa: A Systematic Review. *Frontiers in Neuroscience*, *13*, 23.

Smith, R. E., Tournier, J.-D., Calamante, F., & Connelly, A. (2015). SIFT2: Enabling dense quantitative assessment of brain white matter connectivity using streamlines tractography. *NeuroImage*, *119*, 338–351.

Staempfli, P., Rienmueller, A., Reischauer, C., Valavanis, A., Boesiger, P., & Kollias, S. (2007). Reconstruction of the human visual system based on DTI fiber tracking. *Journal of Magnetic Resonance Imaging: JMRI*, *26*(4), 886–893.

Takemura, H., Caiafa, C. F., Wandell, B. A., & Pestilli, F. (2016). Ensemble Tractography. *PLoS Computational Biology*, *12*(2), e1004692.

Takemura, H., Ogawa, S., Mezer, A. A., Horiguchi, H., Miyazaki, A., Matsumoto, K., Shikishima, K., Nakano, T., & Masuda, Y. (2019). Diffusivity and quantitative T1 profile of human visual white matter tracts after retinal ganglion cell damage. *NeuroImage. Clinical*, *23*, 101826.

Takemura, M. Y., Hori, M., Yokoyama, K., Hamasaki, N., Suzuki, M., Kamagata, K., Kamiya, K., Suzuki, Y., Kyogoku, S., Masutani, Y., & Others. (2017). Alterations of the optic pathway between unilateral and bilateral optic nerve damage in multiple sclerosis as revealed by the combined use of advanced diffusion kurtosis imaging and visual evoked potentials. *Magnetic Resonance Imaging*, *39*, 24–30.

Thomas, C., Ye, F. Q., Irfanoglu, M. O., Modi, P., Saleem, K. S., Leopold, D. A., & Pierpaoli, C. (2014). Anatomical accuracy of brain connections derived from diffusion MRI tractography is inherently limited. *Proceedings of the National Academy of Sciences of the United States of America*, *111*(46), 16574–16579.

Tian, Q., Wintermark, M., Jeffrey Elias, W., Ghanouni, P., Halpern, C. H., Henderson, J. M., Huss, D. S., Goubran, M., Thaler, C., Airan, R., Zeineh, M., Pauly, K. B., & McNab, J. A. (2018). Diffusion MRI tractography for improved transcranial MRI-guided focused ultrasound thalamotomy targeting for essential tremor. *NeuroImage. Clinical*, *19*, 572–580.

Tournier, J.-D., Calamante, F., & Connelly, A. (2007). Robust determination of the fibre orientation distribution in diffusion MRI: non-negativity constrained super-resolved spherical deconvolution. *NeuroImage*, *35*(4), 1459–1472.

Tournier, J.-D., Calamante, F., & Connelly, A. (2012). MRtrix: diffusion tractography in crossing fiber regions. *International Journal of Imaging Systems and Technology*, *22*(1), 53–66.

Tournier, J.-D., Calamante, F., Gadian, D. G., & Connelly, A. (2004). Direct estimation of the fiber orientation density function from diffusion-weighted MRI data using spherical deconvolution. *NeuroImage*, *23*(3), 1176–1185.

Tuch, D. S., Reese, T. G., Wiegell, M. R., Makris, N., Belliveau, J. W., & Wedeen, V. J. (2002). High angular resolution diffusion imaging reveals intravoxel white matter fiber heterogeneity. *Magnetic Resonance in Medicine: Official Journal of the Society of Magnetic Resonance in Medicine / Society of Magnetic Resonance in Medicine*, *48*(4), 577–582.

Turbin, R. E., Thompson, C. R., Kennerdell, J. S., Cockerham, K. P., & Kupersmith, M. J. (2002). A long-term visual outcome comparison in patients with optic nerve sheath meningioma managed with observation, surgery, radiotherapy, or surgery and radiotherapy. *Ophthalmology*, *109*(5), 890–899; discussion 899–900.

Van Essen, D. C., Smith, S. M., Barch, D. M., Behrens, T. E. J., Yacoub, E., Ugurbil, K., & WU-Minn HCP Consortium. (2013). The WU-Minn Human Connectome Project: an overview. *NeuroImage*, *80*, 62–79.

Veraart, J., Fieremans, E., Jelescu, I. O., Knoll, F., & Novikov, D. S. (2016). Gibbs ringing in diffusion MRI. In *Magnetic Resonance in Medicine* (Vol. 76, Issue 1, pp. 301–314). https://doi.org/10.1002/mrm.25866

v. Sántha, K. (1932). Über das Verhalten der primären optischen Zentren bei einseitiger peripherer Blindheit. *Albrecht von Graefes Archiv Für Ophthalmologie*, *129*(2), 224–237.

Wandell, B. A. (2016). Clarifying Human White Matter. *Annual Review of Neuroscience*, *39*, 103–128.

Watanabe, A., Kinouchi, H., Horikoshi, T., Uchida, M., & Ishigame, K. (2008). Effect of intracranial pressure on the diameter of the optic nerve sheath. *Journal of Neurosurgery*, *109*(2), 255–258.

Wu, C.-N., Duan, S.-F., Mu, X.-T., Wang, Y., Lan, P.-Y., Wang, X.-L., & Li, K.-C. (2019). Assessment of optic nerve and optic tract alterations in patients with orbital space-occupying lesions using probabilistic diffusion tractography. *International Journal of Ophthalmology*, *12*(8), 1304–1310.

Xie, G., Zhang, F., Leung, L., Mooney, M. A., Epprecht, L., Norton, I., Rathi, Y., Kikinis, R., Al-Mefty, O., Makris, N., Golby, A. J., & O'Donnell, L. J. (2020a). Anatomical assessment of trigeminal nerve tractography using diffusion MRI: a comparison of acquisition b-values and single- and multi-fiber tracking strategies. *NeuroImage:Clinical*, *25*, 102160.

Xie, G., Zhang, F., Leung, L., Mooney, M. A., Epprecht, L., Norton, I., Rathi, Y., Kikinis, R., Al-Mefty, O., Makris, N., Golby, A. J., & O'Donnell, L. J. (2020b). Anatomical assessment of trigeminal nerve tractography using diffusion MRI: A comparison of acquisition b-values and single- and multi-fiber tracking strategies. *NeuroImage. Clinical*, *25*, 102160.

Yoshino, M., Abhinav, K., Yeh, F.-C., Panesar, S., Fernandes, D., Pathak, S., Gardner, P. A., & Fernandez-Miranda, J. C. (2016). Visualization of Cranial Nerves Using High-Definition Fiber

Tractography. *Neurosurgery*, *79*(1), 146–165.

Zhang, F., Cetin Karayumak, S., Hoffmann, N., Rathi, Y., Golby, A. J., & O'Donnell, L. J. (2020). Deep white matter analysis (DeepWMA): fast and consistent tractography segmentation. *Medical Image Analysis*, 101761.

Zhang, F., Ning, L., O'Donnell, L. J., & Pasternak, O. (2019). MK-curve - Characterizing the relation between mean kurtosis and alterations in the diffusion MRI signal. *NeuroImage*, *196*, 68–80.

Zhang, F., Noh, T., Juvekar, P., Frisken, S. F., Rigolo, L., Norton, I., Kapur, T., Pujol, S., Wells, W., 3rd, Yarmarkovich, A., Kindlmann, G., Wassermann, D., San Jose Estepar, R., Rathi, Y., Kikinis, R., Johnson, H. J., Westin, C.-F., Pieper, S., Golby, A. J., & O'Donnell, L. J. (2020). SlicerDMRI: Diffusion MRI and Tractography Research Software for Brain Cancer Surgery Planning and Visualization. *JCO Clinical Cancer Informatics*, *4*, 299–309.

Zhang, F., Wu, Y., Norton, I., Rathi, Y., Golby, A. J., & O'Donnell, L. J. (2019). Test–retest reproducibility of white matter parcellation using diffusion MRI tractography fiber clustering. *Human Brain Mapping*, *28*, 173.

Zhang, F., Wu, Y., Norton, I., Rigolo, L., Rathi, Y., Makris, N., & O'Donnell, L. J. (2018). An anatomically curated fiber clustering white matter atlas for consistent white matter tract parcellation across the lifespan. *NeuroImage*, *179*, 429–447.

Zhang, F., Xie, G., Leung, L., Mooney, M. A., Epprecht, L., Norton, I., Rathi, Y., Kikinis, R., Al-Mefty, O., Makris, N., Golby, A. J., & O'Donnell, L. J. (2020). Creation of a novel trigeminal tractography atlas for automated trigeminal nerve identification. *NeuroImage*, *220*, 117063.

Zolal, A., Sobottka, S. B., Podlesek, D., Linn, J., Rieger, B., Juratli, T. A., Schackert, G., & Kitzler, H. H. (2017). Comparison of probabilistic and deterministic fiber tracking of cranial nerves. *Journal of Neurosurgery*, *127*(3), 613–621.

Supplementary 1: Experiment to determine best-performing tractography parameters

Different parameter settings will significantly influence the results of tractography (Parizel et al., 2007). In order to compare multiple tractography algorithms fairly, we first perform an experiment to determine the best-performing parameters for each tractography method, as in our previous work (Xie et al., 2020a).

The key parameters that may affect the RGVP tractography results were tested in each compared method. Detailed information about the parameters is shown in Table S1. For the UKF tractography methods (UKF-1T and UKF-2T), the major parameters include *seedingFA*, *stoppingFA*, *Qm*, and *Ql*. Tractography is seeded in all voxels within RGVP seeding mask (as shown in Figure 3a), where FA is greater than the *seedingFA* threshold value. Tracking stops in voxels where the FA value falls below the *stoppingFA* threshold value. During the tracking, the UKF tractography methods use the *Qm* parameter to control process noise for angles/direction, and use the *Ql* parameter to control process noise for eigenvalues. For the CSD-based methods, the major parameters include *seedCutoff*, *stopCutoff* and *maximumAngle*. Tractography is seeded in the voxels within the mask where the FOD amplitude is higher than the *seedCutoff* threshold value. Tracking stops when the direction of fiber tracking turns through an angle higher than the *maximumAngle* threshold value or the current voxel FOD amplitude falls below the *stopCutoff* threshold value.

In the experiment, in each tractography method, we tested a range of values that were large enough to cover possible settings for each parameter (see Table S1). For each of the 57 subjects (detailed information in Section 2.1) under study, all possible parameter combinations within the selected value ranges were tested. (All other parameters follow the default value suggested by the software.) For each parameter combination, after tractography seeding, we performed ROI-based RGVP fiber selection (as in Section 2.2.2), and we calculated the overall reconstruction rate of RGVP subdivisions (i.e., the percentage of subjects where all four RGVP subdivisions were successfully reconstructed, as in Section 2.3.1). A total of 12,768 putative RGVPs were reconstructed (224 parameter combinations × 57 subjects) for each of the UKF tractography methods, and a total of 20,520 putative RGVPs were reconstructed in each of the CSD-based tractography methods based tractography method (360 parameter combinations × 57 subjects) were produced. Then, the best-performing parameter setting was set to those that generated the highest overall reconstruction rate. For each of the SD-Stream and iFOD1 methods, we found two settings that generated the highest overall reconstruction rate, and we chose the setting that is closer to the default setting.

Table S1. Key parameters and values tested for each tractography method

Tractography method	**Key parameter**	**Description**	**Values tested**
SD-Stream and iFOD1	seedCutoff	Minimum FOD amplitude for seeding tracking	0.005 - 0.050
	stopCutoff	FOD amplitude cutoff for terminating tracking	Equal to or 0.001 lower than the seedCutoff value
	maximumAngle	Maximum angle between successive step	5 - 90
UKF-1T and UKF 2T	seedingFA	Minimum FA for seeding tracking	0.01 - 0.04
	stoppingFA	FA cutoff for terminating tracks	Equal to or 0.01 lower than seedingFA

	Qm	Process noise for angles or direction during model fitting	0.001 - 0.004
	Ql	Process noise for eigenvalues during model fitting	50 - 350